

## ORIGINAL RESEARCH ARTICLE

# Exploring complex spectroscopic characteristics of (Ag)<sub>x</sub>/CuTl-1223 nanoparticles-superconductor composites through impedance and electric modulus analysis

M. Mumtaz<sup>1,\*</sup>, Mubasher<sup>2,†</sup>, Liaqat Ali<sup>1,†</sup>, Mehwish Hassan<sup>3</sup>, Abrar A. Khan<sup>1</sup>, Haris Ahmed Abbasi<sup>1</sup>, M. Nasir Khan<sup>4</sup>

<sup>1</sup> Materials Research Laboratory, Department of Physics, Faculty of Sciences, International Islamic University, Islamabad 44000, Pakistan

<sup>2</sup> Department of Physics, Faculty of Engineering and Applied Sciences, Riphah International University, I-14 Islamabad 44000, Pakistan

<sup>3</sup> Department of Sciences and Humanities, National University of Computer and Emerging, Sciences, Islamabad 44000, Pakistan

<sup>4</sup> Central Diagnostic Laboratory, Physics Division PINSTECH, Islamabad 45500, Pakistan

\* Corresponding author: M. Mumtaz, mmumtaz75@yahoo.com

† Authors contributed equally to this work.

## ABSTRACT

This study elucidates influence of silver (Ag) nanoparticles (NPs) on ac-conduction properties within the superconductive phase of Cu<sub>0.5</sub>Tl<sub>0.5</sub>Ba<sub>2</sub>Ca<sub>2</sub>Cu<sub>3</sub>O<sub>10-δ</sub> (CuTl-1223). The Ag NPs were prepared by sol-gel method and CuTl-1223 superconducting phase was prepared by conventional solid-state reaction method. The different weight percentages (wt.%) of Ag NPs were mixed with CuTl-1223 superconducting matrix in order to obtain (Ag)<sub>x</sub>/CuTl-1223;  $x = 0 \sim 4.0$  wt.% nanoparticles-superconductor composites. Complex impedance spectroscopy (CIS) and complex electric modulus spectroscopy (CEMS) were conducted to probe the impact of Ag NPs addition along the grain-boundaries of the bulk CuTl-1223 superconducting matrix and on the resistive and capacitive contributions to the total impedance at different T (K) and f (Hz) values.

**Keywords:** Ag nanoparticles; CuTl-1223 superconducting phase; (Ag)<sub>x</sub>/CuTl-1223 composites; complex impedance spectroscopy; complex electric modulus spectroscopy

**PACS codes:** 74.25. F-; 74.25.-q; 74.81. Bd; 74.72.-h

## 1. Introduction

Although high temperature superconductors (HTSCs) have undergone extensive synthesis and characterization, the literature survey reveals, a limited exploration of their ac-conduction behavior, particularly when employing dielectric, impedance and modulus measurements. Thus this study focus on the ac-conduction phenomenon of HTSCs concentrating on specific applied frequencies and temperatures. This study can provide an interpretation regarding the role of the grains and grain-boundaries in ac-conduction

### ARTICLE INFO

Received: 26 September 2023 | Accepted: 20 October 2023 | Available online: 22 December 2023

### CITATION

Mumtaz M, Mubasher, Ali L, et al. Exploring complex spectroscopic characteristics of (Ag)<sub>x</sub>/CuTl-1223 nanoparticles-superconductor composites through impedance and electric modulus analysis. *Micromaterials and Interfaces* 2023; 1(1): 2313. doi: 10.54517/mi.v1i1.2313

### COPYRIGHT

Copyright © 2023 by author(s). *Micromaterials and Interfaces* is published by Asia Pacific Academy of Science Pte. Ltd. This is an Open Access article distributed under the terms of the Creative Commons Attribution License (<https://creativecommons.org/licenses/by/4.0/>), permitting distribution and reproduction in any medium, provided the original work is cited.

process. The relaxation processes and the role of the grains and grain-boundaries in granular materials on the ac-conduction properties have generally been explored by the complex impedance spectroscopy (CIS) and the complex electric modulus spectroscopy (CEMS)<sup>[1-3]</sup>. CIS measurements are used to determine the resistive contribution to impedance however they fall short in considering the smaller contribution of the capacitive reactance to the impedance in granular materials<sup>[4,5]</sup>. To address this CEMS technique is commonly employed enabling the measurement of small contribution of capacitive reactance to the impedance of the granular materials<sup>[6,7]</sup>. The grain, grain-boundaries, interfaces and different other defects (impurities, pores, cracks, etc.) can affect the ac-conduction properties of the granular materials<sup>[8]</sup>. The insertion of nanostructures of various materials, sizes and shapes can modify the morphology and nature of the grain-boundaries in the bulk materials<sup>[9,10]</sup>. Therefore, the investigation of the effects of the insertion of different nanostructures across the grain-boundaries for the ac-conduction properties can be useful to tune the electrical transport properties of the bulk materials for different practical applications.

The effects of introducing MgO NPs on the ac-conduction properties of  $\text{Cu}_{0.25}\text{Tl}_{0.75}\text{Ba}_2\text{Ca}_3\text{Cu}_4\text{O}_{12-\delta}$  superconducting phase was investigated at different temperatures from 113 K to 300 K and frequencies from 100 Hz to 4 MHz. A strong correlation between the ac-conduction properties and the frequency, temperature and MgO NPs content was observed. The variation in ac-conduction revealed the Debye-like nature of the relaxation process in these nanocomposites<sup>[11]</sup>. CIS and CEMS measurements were employed to study the influence of  $\text{Co}_3\text{O}_4$  NPs addition on different aspects of CuTl-1223 superconducting matrix. The non-Debye type relaxation was observed in these composites. The impedance was observed to be decreased with the addition of these NPs in CuTl-1223 superconducting matrix<sup>[12]</sup>. Similarly, the effects of insertion of  $\text{MnFe}_2\text{O}_4$  and Cu NPs in CuTl-1223 superconducting matrix were explored by impedance and modulus spectroscopic studies at different temperature values from 78 K to 253 K and frequencies values from 20 Hz to 10 MHz. It was observed that grains as well as grain-boundaries affect the transport mechanism in these composites. The relaxation phenomenon of non-Debye type was observed in these composites by CIS and CEMS measurements. The resistance and reactance of the grains gave lower values as compared to that of grain-boundaries. This is the confirmation of good conducting nature of grains and poor conduction properties of grain-boundaries<sup>[13-15]</sup>. The effects of addition of different oxides, ferrites and metallic NPs on the superconducting as well as ac-condition properties of various bulk HTSCs were explored<sup>[16-21]</sup>. But still more work is needed to completely understand the factors affecting the ac-conducting properties of the bulk HTSCs for the practical applications.

Therefore, in the current study, the influence of Ag NPs addition on ac-conduction processes in CuTl-1223 superconducting phase were explored via CIS and CEMS measurements. As Ag is one of the best conducting element, therefore, it was expected that the addition of Ag NPs will significantly improve the conducting nature of the grain-boundaries of bulk CuTl-1223 superconductor. So, the role of Ag NPs addition on the ac-conduction properties was probed via CIS and CEMS measurements of  $(\text{Ag})_x/\text{CuTl-1223}$  composites. This study can help to chart out the parameters influencing the ac-conduction mechanism in the nanostructures added HTSCs.

## 2. Samples synthesis and characterization

The Ag NPs were synthesized by sol gel method. The process was started with the preparation of solutions of distilled water with citric acid and hydrated silver nitrate added in ethanol. These solutions were mixed in one beaker and ammonia was added drop wise to maintain 9 pH. This solution was stirred during heating process at 80 °C to form a gel. After drying this gel in an oven at 100 °C, it was ground for one hour. Then, the powder was annealed at 900 °C for 4 h to get Ag NPs. The calculated masses of solid powders of different compounds such as  $\text{Cu}_2(\text{CN})_2$ ,  $\text{Ca}(\text{NO}_3)_2$  and  $\text{Ba}(\text{NO}_3)_2$  were combined and mechanically ground for about 2

h using mortar and pestle. The prepared mixture was heat treated at 860 °C for 24 h in a pre-heated chamber furnace. Then calculated amounts of Ag NPs and thallium oxide ( $Tl_2O_3$ ) were added in the precursor. Finally, the pellets were formed by hydraulic press and wrapped in gold capsules for the purpose of sintering in pre-heated chamber furnace at 860 °C for about 10 min. In this way, the desired  $(Ag)_x/CuTi-1223$ ;  $x = 0 \sim 4.0$  wt.% composites were obtained. The ac-conduction measurements (i.e., CIS and CEMS) of  $(Ag)_x/CuTi-1223$ ;  $x = 0 \sim 4.0$  wt.% NPs superconductor composites were obtained with the help of Hewlett-Packard 4294A LCR Meter using two-point probe method in the frequency range of 40 Hz to 100 MHz at different T (K) from 78 K to 253 K. The size of samples used for LCR measurements was  $1.25 \times 2.4 \times 2.1$  mm<sup>3</sup>.

### 3. Results and discussion

#### 3.1. X-ray diffraction (XRD)

The structural properties of Ag NPs added CuTi-1223 superconducting phase have been studied by X-ray diffraction (XRD). The XRD spectra of  $(Ag)_x/CuTi-1223$  nanocomposites with  $x = 0$  and 2.0 wt.% and Ag NPs in its inset are shown by **Figure 1**. All noticeable peaks were perfectly indexed following the p4/mmm space group and tetragonal structure in computer software for structure refinement ‘MDI Jade’ with latest international center for diffraction data (ICDD). The low intensity peaks appearing in the spectra can be attributed to other superconducting phases and impurities in the matrix. A minor improvement was observed along c-axis of host unit cell which may be linked to the improved oxygen ( $O_s$ ) content and stresses exerted by Ag NPs dispersed over inter-granular spaces. No alteration was observed in the crystal structure of superconducting matrix with the addition of Ag NPs. This was the confirmation of the fact that these NPs had not penetrated into the unit cell of the host rather they occupied available spaces at inter-granular sites of host. In the inset of **Figure 1**, the XRD plot of metallic Ag NPs is given. The prominent peaks observed with (hkl) values (111), (200) and (220) perfectly match the ICDD record and follow FCC structure. The sharpness of the peaks and absence of impurity phases indicate perfect crystallinity in NPs structure. The average crystallite size of Ag NPs is found to be 35 nm as calculated by Sherrer’s formula. Furthermore, the surface morphology, and elemental composition of Ag NPs added CuTi-1223 superconducting phase have already been reported in our previous studies<sup>[22–26]</sup>. The increase in the mass densities due to added Ag NPs in the host superconductor is expected to reduce the porosity by stuffing and filling of pores, voids and cracks present in the samples<sup>[27]</sup>.

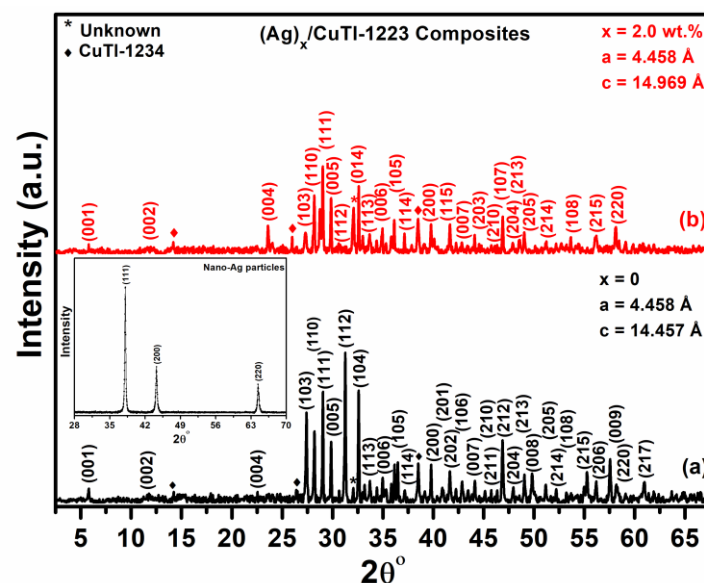


**Figure 1.** The representative XRD spectra of  $(Ag)_x/CuTi-1223$  composites;  $x = 0$  and 2.0 wt.% composites. Inset contain XRD spectrum of Ag nanoparticles.

### 3.2. Resistivity ( $\rho$ ) vs. temperature ( $T$ ) measurements

The dc-resistivity vs. temperature curves of the superconducting nanocomposites of  $(\text{Ag})_x/\text{CuTl-1223}$ ,  $x = 0$  and 2.0 wt.% are plotted in **Figure 2**. Ag NPs showed a remarkable effect by decreasing the resistivity of the normal state  $\rho_n$  ( $\Omega \text{ m}$ ) to much lower values and a great increase in the characteristic critical temperature  $T_c(0)$  from 73 to 103K for given concentrations. As confirmed in the structural analysis that metallic Ag NPs occupy pores and voids at grain boundaries, so they become coupling agents between crystallites and enhance the volume fraction of the superconducting regions in the materials. The enhancement in the inter-crystallite connectivity with metallic Ag NPs reduces the resistive losses across grain boundaries. The charge carriers in the superconducting state are in the form of pairs of electrons called cooper pairs, which show dissipation less transport in superconducting state. When these pairs of electrons from the superconducting region reach the grain boundaries and interact with non-superconducting metallic Ag NPs, their pairing interaction slightly reduce but because of links established by metallic NPs of dominantly improved conductivity. In the inset of **Figure 2** the derivative of the resistivity curves have been plotted against the temperature for the same compositions. A single step sharp transition is observed for the superconducting nanocomposites in the region where intra-grain superconductivity is established and inter-grain space is non-superconducting. The peak positions clearly depict the rise in mean field critical temperature [ $T_c^{\text{mf}}(\text{K})$ ] from 99 to 115K after addition of metallic Ag NPs.

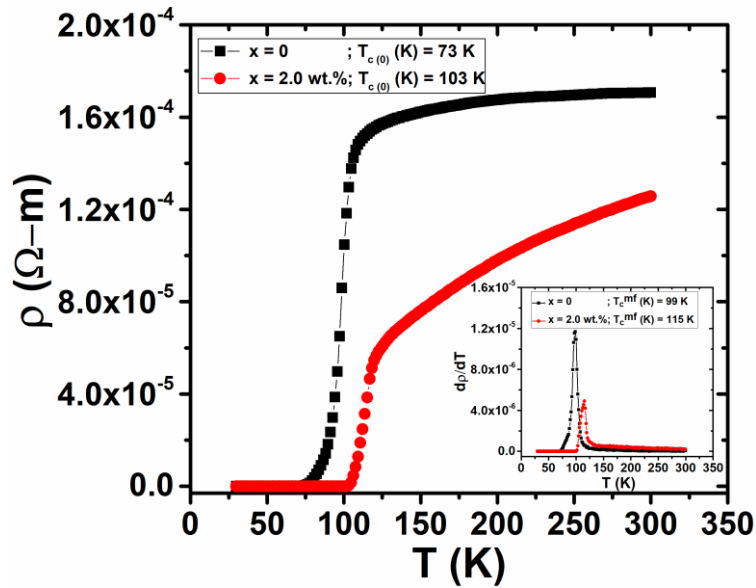


**Figure 2.** The representative dc resistivity ( $\rho$ ) vs temperature  $T$  (K) for  $(\text{Ag})_x/\text{CuTl-1223}$  composites;  $x = 0$  and 2.0 wt.% composites. Inset contain derivatives of resistivity vs  $T$ (K).

### 3.3. Complex impedance spectroscopy (CIS)

The CIS technique provides a valuable insights into how relaxation processes occur in different solid materials at various values of applied frequency and temperature<sup>[28,29]</sup>. The CIS technique is also applied to explore the dynamics of the bound charges present in the bulk and interfacial regions of the polycrystalline solids<sup>[19]</sup>. As the behavior of grains and grain-boundaries differs when subjected to an applied sinusoidal perturbation, so the CIS method can help in distinguishing their respective contribution to the ac-conduction processes<sup>[30]</sup>. The complex impedance is denoted by  $Z^*$ , while its real and imaginary parts are denoted by  $Z'$  and  $Z''$  respectively. It is mathematically given by the following Equation (1);

$$Z^* = Z'_{\text{real}} + jZ''_{\text{imag}} \quad (1)$$

where 'j' is the complex number that represents the imaginary part of the complex impedance.

The complex impedance ( $Z^*$ ) from this equivalent circuit can be given as follows;

$$Z^* = \frac{1}{\frac{1}{R_g} + j\omega C_g} + \frac{1}{\frac{1}{R_{gb}} + j\omega C_{gb}}$$

$$Z^* = \frac{R_g}{1 + j\omega C_g R_g} + \frac{R_{gb}}{1 + j\omega C_{gb} R_{gb}}$$

$$Z^* = \left( \frac{R_g}{1 + j\omega R_g C_g} \times \frac{1 - j\omega R_g C_g}{1 - j\omega R_g C_g} + \frac{R_{gb}}{1 + j\omega R_{gb} C_{gb}} \times \frac{1 - j\omega R_{gb} C_{gb}}{1 - j\omega R_{gb} C_{gb}} \right)$$

$$Z^* = \left[ \left( \frac{R_g}{1 + (\omega R_g C_g)^2} \right) + \left( \frac{R_{gb}}{1 + (\omega R_{gb} C_{gb})^2} \right) \right] + j \left[ R_g \left( \frac{\omega R_g C_g}{1 + (\omega R_g C_g)^2} \right) + R_{gb} \left( \frac{\omega R_{gb} C_{gb}}{1 + (\omega R_{gb} C_{gb})^2} \right) \right] \quad (2)$$

By comparing the Equation (2) with Equation (1), we get;

$$Z' = \left( \frac{R_g}{1 + (\omega R_g C_g)^2} \right) + \left( \frac{R_{gb}}{1 + (\omega R_{gb} C_{gb})^2} \right) \quad (3)$$

$$Z'' = R_g \left( \frac{\omega R_g C_g}{1 + (\omega R_g C_g)^2} \right) + R_{gb} \left( \frac{\omega R_{gb} C_{gb}}{1 + (\omega R_{gb} C_{gb})^2} \right) \quad (4)$$

The variation of  $Z'$  vs frequency of Ag NPs added CuTl-1223 superconductor composites at different temperature from 78 K–253 K are shown in **Figure 3a–e**. The higher values of  $Z'$  at lower frequency region highlights the dominant resistive contribution to the impedance of these composites<sup>[31]</sup>. This resistive behaviour can be attributed to the enhanced carriers' scattering across the grain-boundary regions. At higher applied frequencies, all curves of  $Z'$  vs.  $f$  (Hz) are merged for all values of temperatures. This behaviour can be attributed to the absence of restoring force, which enables greater mobility of charge carriers according to the applied frequency<sup>[31]</sup>. The value of  $Z'$  increases gradually with the increase of temperature at 40 Hz as shown in the insets of **Figure 3a–e**. The variation in the value of  $Z'_{\text{Max}}$  with  $T$  (K) for different concentration of Ag NPs in CuTl-1223 matrix is shown in **Figure 3f**. The rising trend is also evident with increasing contents of Ag NPs in CuTl-1223 superconducting matrix. The observed increase in the values of  $Z'$  with temperature can be related to the increased scattering of carriers across the grain-boundaries, which is further enhanced with the addition of metallic Ag NPs in CuTl-1223 superconducting phase.

Similarly, the changes in  $Z''$  with frequency across a temperature range varied from 78 K to 253 K for different concentrations of Ag NPs introduced in CuTl-1223 superconducting phase is represented by **Figure 4a–f**. It is evident from these plots that the values of  $Z''$  have increased as frequency rises until it gained its maximum  $Z''_{\text{Max}}$ , after which they begin to decline with further increase in frequency. The rising pattern for  $Z''_{\text{Max}}$  with temperature, observed for varying percentages of Ag NPs in CuTl-1223 superconducting phase can be visualized in the insets of **Figure 4a–e**. The turning point in  $Z''$  is the part where transition of long range to short range mobility of charge carriers occurred. This is owed to the hopping and relaxation mechanism of ac-conduction process of charge carriers in material. The elevation in the values of  $Z''_{\text{Max}}$  with both temperature and Ag NPs contents is clearly shown in **Figure 4f**. The increase in  $Z''_{\text{Max}}$  with both temperature and addition of Ag NPs contents can be attributed to the enhanced resistive nature of grain-boundaries with increasing temperature due to conducting nature of metallic Ag NPs added across the grain-boundaries of the host CuTl-1223 superconducting matrix. The peaks between  $Z''$  and frequency have been observed to be shifted to higher frequency with increasing temperature. This that multiple relaxation processes are going on in these samples. The region a under each curve, spanning between  $Z''$  and frequency gives the range of frequency in which the mobility of charges is primarily influenced by the long-range hopping mechanism. The carriers face the maximum barrier potential at the peak frequency. The peak of each curve signifies the threshold frequency at which the charge carriers can transit from short range mobility mode to long range mobility mode. This behaviour confirms that the ac-conduction in the composites is effected by thermally activated hopping

mechanism<sup>[32]</sup>. The sharpness of peaks observed in these of  $Z'$  vs  $f$  (Hz) curves shows actual dielectric relaxation mechanism, whereas the widening of these peaks can be due to distribution of relaxation times<sup>[33]</sup>. The shifting of peak positions observed in these graphs can precisely be explained by the following Equation (5).

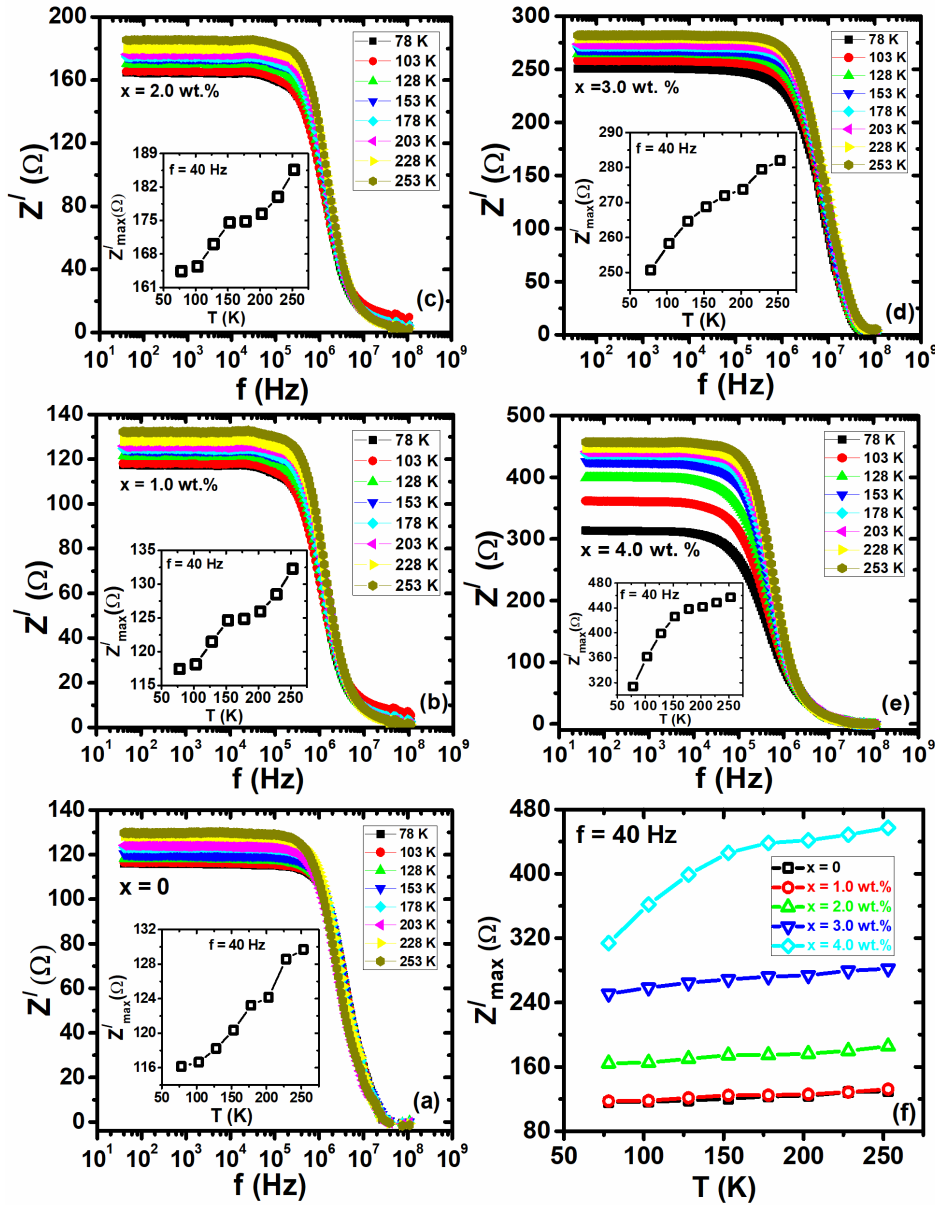


**Figure 3.** Variation in real part of impedance ( $Z'$ ) versus test frequency  $f$  (Hz) from 40 Hz to 10 MHz at different operating temperatures  $T$  (K) from 78 K to 253 K for  $(Ag)_x/CuTiI-1223$  composites with (a)  $x = 0$ , (b)  $x = 1.0$  wt.%, (c)  $x = 2.0$  wt.%, (d)  $x = 3.0$  wt.%, (e)  $x = 4.0$  wt.% each with inset of variation in  $Z'_{Max}$  versus  $T$  (K), and (f) Combined variation of  $Z'_{Max}$  versus  $T$  (K) for  $(Ag)_x/CuTiI-1223$ ;  $x = 0, 1.0, 2.0, 3.0$  and  $4.0$  wt.% composites.

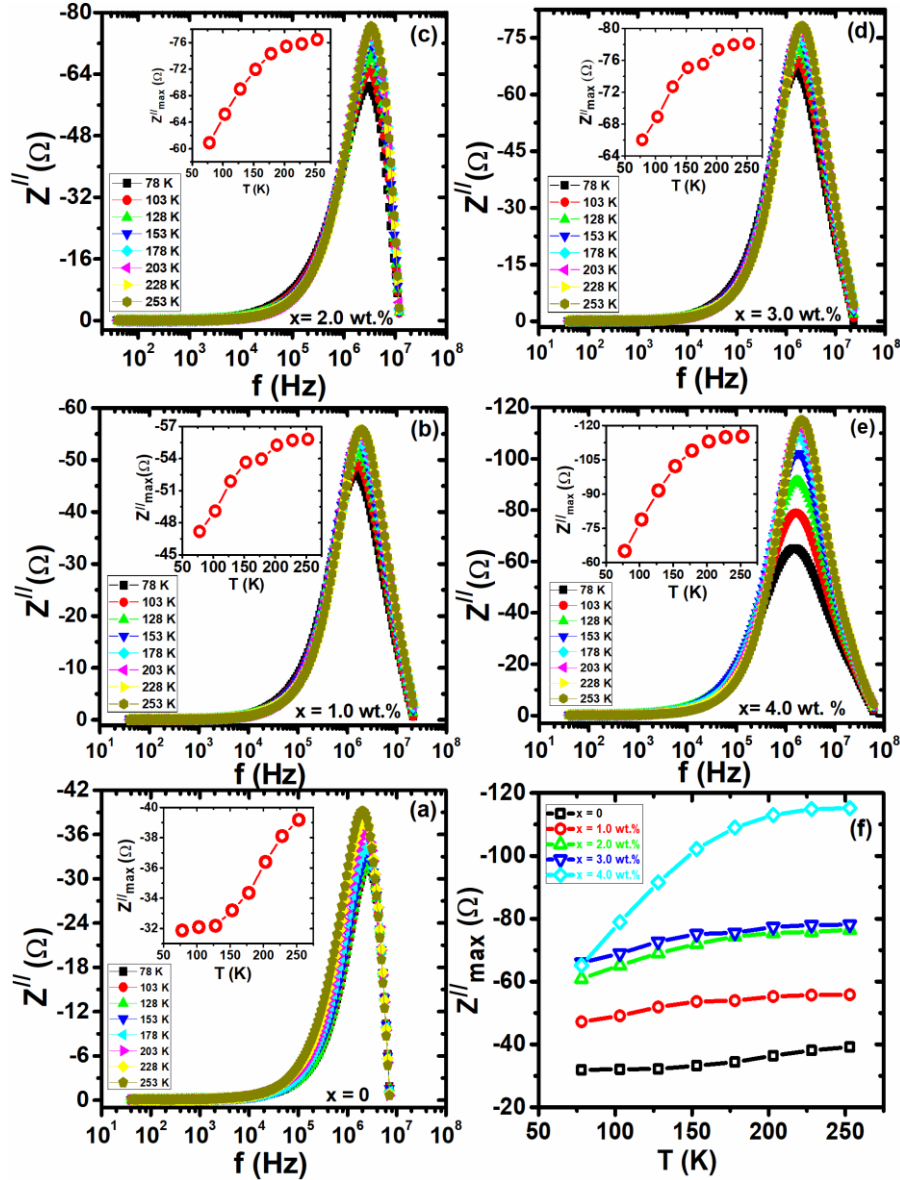


**Figure 4.** Variation in imaginary part of impedance ( $Z''$ ) versus test frequency  $f$  (Hz) from 40 Hz to 10 MHz at different operating temperatures  $T$  (K) from 78 K to 253 K for  $(\text{Ag})_x/\text{CuTi-1223}$  composites with (a)  $x = 0$ , (b)  $x = 1.0$  wt.%, (c)  $x = 2.0$  wt.%, (d)  $x = 3.0$  wt.%, (e)  $x = 4.0$  wt.% each with inset of variation in  $Z''_{\text{Max}}$  versus  $T$  (K), and (f) combined variation in  $Z''_{\text{Max}}$  versus  $T$  (K) for  $(\text{Ag})_x/\text{CuTi-1223}$ ;  $x = 0, 1.0, 2.0, 3.0$  and  $4.0$  wt.% composites.

$$\omega = 2\pi f = \frac{1}{\tau} = \frac{1}{C_{gb}R_{gb}} \quad (5)$$

According to this Equation (5), the shifting in peak positions can be associated with the variation in the values of  $R_{gb}$  and  $C_{gb}$  with temperature and Ag NPs contents. The peaks shifted towards the low frequency is due to the settlement of Ag NPs at the grain-boundaries of the superconductor which enhanced the charge accumulation at grain-boundaries and suppressed the tunnelling of electrons between grain and grain-boundaries. At this stage, the grain-boundaries offered more  $R_{gb}$  resistance and  $C_{gb}$  capacitance. This is also an evidence of relaxation phenomenon of non-Debye type nature in these composites<sup>[34]</sup>.

The Nyquist plots, showing the relation between  $Z'$  and  $Z''$  for different concentrations of Ag NPs at different temperature values ranging from 78 K to 253 K are shown in **Figure 5a–e**. From these Nyquist plots, we can determine the grains' resistance ( $R_g$ ) from left intercepts on  $Z'$  axis, and total resistance  $R$  ( $R = R_{gb} + R_g$ ) can be determined from right intercepts on  $Z'$  axis, respectively. An equivalent circuit is designed to account

for the involvement of grains and of grain-boundaries to the ac-conduction processes in the material as depicted by **Figure 5f**. In the equivalent circuit, the grains' resistance ( $R_g$ ) and grains' capacitance ( $C_g$ ) are parallel to each other and similarly the grain-boundaries' resistance ( $R_{gb}$ ) is also parallel to the grain-boundaries' capacitance ( $C_{gb}$ ), whereas both parallel sets of circuit are mutually connected in series. **Table 1** shows the values of  $R_g$  and  $R_{gb}$  calculated from these Nyquist plots. The higher values of resistance of grains and grain-boundaries with increasing temperature highlights the conducting nature of the grains and grain-boundaries. On comparison of resistance originating from both the regions shows that the grains exhibit lower resistance, while grain-boundaries exhibit more resistance. The values of  $C_g$  and  $C_{gb}$  can be determined from the following Equation (6) and Equation (7), respectively.

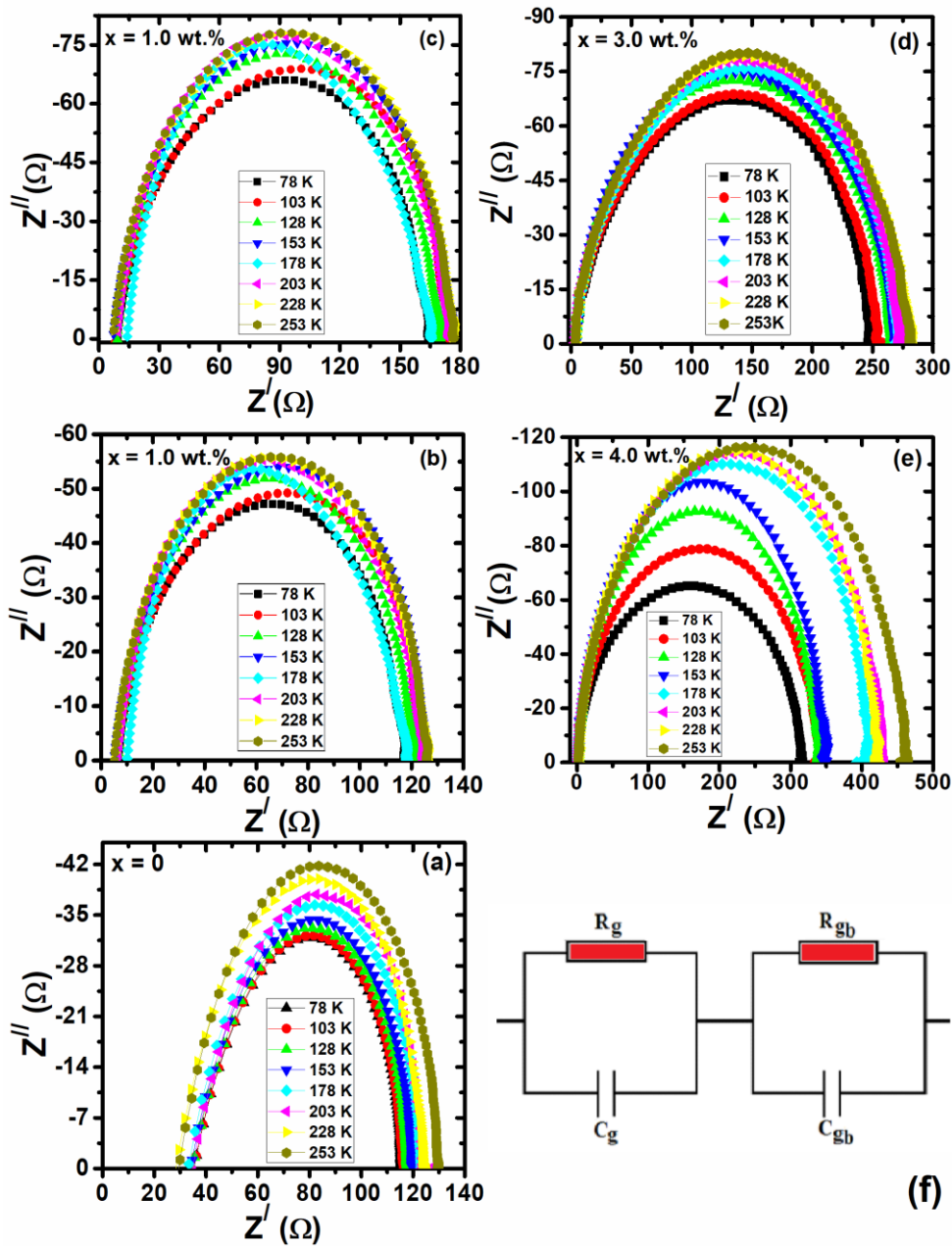


**Figure 5.** Nyquist plots between  $Z'$  and  $Z''$  at different operating temperatures  $T$  (K) from 78 K to 253 K for  $(Ag)_x/CuTi-1223$  composites with (a)  $x = 0$ , (b)  $x = 1.0$  wt.%, (c)  $x = 2.0$  wt.%, (d)  $x = 3.0$  wt.%, (e)  $x = 4.0$  wt.%, and (f) equivalent circuit containing  $R_g$ ,  $R_{gb}$ ,  $C_g$  and  $C_{gb}$ .

**Table 1.** Calculated values of ‘ $R_g$ ’ and ‘ $R_{gb}$ ’ of (Ag) $_x$ /CuTi-1223,  $x = 0, 1.0, 2.0, 3.0$  and  $4.0$  wt.% composites at various temperatures.

(Ag) $_x$ /CuTi-1223, $x = 0, 1.0, 2.0, 3.0$ and $4.0$ wt.% composites										
T (K)	$x = 0$		$x = 1.0$		$x = 2.0$		$x = 3.0$		$x = 4.0$	
	$R_g$	$R_{gb}$	$R_g$	$R_{gb}$	$R_g$	$R_{gb}$	$R_g$	$R_{gb}$	$R_g$	$R_{gb}$
78	36.3	115.3	6.69	117.5	9.36	164.5	4.61	247.7	1.51	316.5
103	36.1	115.8	5.96	123.9	8.33	173.4	4.13	252.6	1.53	338.6
128	35.5	117.5	6.82	121.1	9.55	169.6	4.45	264.5	1.57	337.4
153	34.6	119.7	5.31	125.6	7.29	175.8	4.46	268.7	1.64	349.0
178	33.3	123.3	10.0	118.1	14.0	165.4	3.58	270.9	1.80	404.5
203	36.9	123.3	6.80	124.4	9.51	174.2	3.52	273.3	1.81	428.1
228	29.5	123.4	5.25	125.8	7.57	176.6	3.59	280.1	1.75	419.7
253	29.8	129.4	5.38	126.2	7.41	176.6	3.48	281.2	1.81	461.8

$$f_{max} = \frac{1}{2\pi R_g C_g} \tag{6}$$

$$f_{max} = \frac{1}{2\pi R_{gb} C_{gb}} \tag{7}$$

The significant change in the Nyquist plots shape of these nanocomposites with increasing temperature is indicative for multi-Debye relaxation nature of these nanocomposites<sup>[35]</sup>. An important parameter referred as blocking factor ( $\alpha_R$ ) can be employed to assess the role of grain-boundaries in ac-conduction of material and it can be calculated by using the following Equation (8).

$$\alpha_R = \frac{R_{gb}}{R_g + R_{gb}} \tag{8}$$

The rising trend in the values of  $\alpha_R$  with increasing Ag NPs concentration in the host CuTi-1223 superconducting matrix at different temperatures can be seen in **Figure 6**. The values of  $\alpha_R$  provide the crucial insights related to the amount of restricted charge carriers in the potential wells present at the grain-boundaries promoted by inclusion of Ag NPs in the bulk of the host CuTi-1223 superconducting phase<sup>[36,37]</sup>.

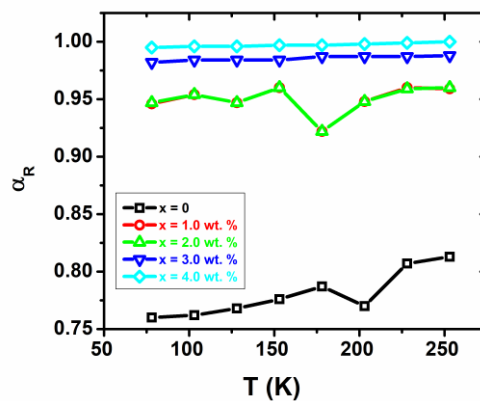


**Figure 6.** Blocking factor ( $\alpha_R$ ) as a function of  $T$  (K) for (Ag) $_x$ /CuTi-1223;  $x = 0, 1.0, 2.0, 3.0$  and  $4.0$  wt% composites.

### 3.4. Complex electric modulus spectroscopy (CEMS)

The CEMS is a technique used to discern the individual contributions of grains and grain-boundaries towards the total impedance of the polycrystalline substances<sup>[38]</sup>. Mainly, components offering equivalent resistance but different capacitance can easily be segregated by using CEMS. The CEMS data can more conveniently analyzed by using an equivalent circuit that consists of two sub-circuits each for grains and grain-

boundaries. The complex modulus is represented by  $M^*$ , while its real part is denoted by  $M'$  and imaginary part is represented by  $M''$ . Mathematically, it can be written as in Equation (9) below<sup>[39]</sup>.

$$M^* = M' + jM'' = j\omega CZ^* \quad (9)$$

By substituting  $Z^*$  in terms of  $R_g$ ,  $R_{gb}$ ,  $C_g$  and  $C_{gb}$  in above Equation (9),  $M^*$  will become;

$$M^* = j\omega C_o \left( \frac{R_g}{1 + j\omega C_g R_g} + \frac{R_{gb}}{1 + j\omega C_{gb} R_{gb}} \right) \quad (10)$$

Equation (10) can further be simplified as;

$$M^* = \left[ \frac{C_o}{C_g} \left( \frac{(\omega C_g R_g)^2}{1 + (\omega C_g R_g)^2} \right) + \frac{C_o}{C_{gb}} \left( \frac{(\omega C_{gb} R_{gb})^2}{1 + (\omega C_{gb} R_{gb})^2} \right) \right] + j \left[ \frac{C_o}{C_g} \left( \frac{\omega C_g R_g}{1 + (\omega C_g R_g)^2} \right) + \frac{C_o}{C_{gb}} \left( \frac{\omega C_{gb} R_{gb}}{1 + (\omega C_{gb} R_{gb})^2} \right) \right] \quad (11)$$

By comparing Equation (9) and Equation (11), we get;

$$M' = \left[ \frac{C_o}{C_g} \left( \frac{(\omega C_g R_g)^2}{1 + (\omega C_g R_g)^2} \right) + \frac{C_o}{C_{gb}} \left( \frac{(\omega C_{gb} R_{gb})^2}{1 + (\omega C_{gb} R_{gb})^2} \right) \right] \quad (12)$$

$$M'' = \left[ \frac{C_o}{C_g} \left( \frac{\omega C_g R_g}{1 + (\omega C_g R_g)^2} \right) + \frac{C_o}{C_{gb}} \left( \frac{\omega C_{gb} R_{gb}}{1 + (\omega C_{gb} R_{gb})^2} \right) \right] \quad (13)$$

where  $C_o$  is the geometrical capacitance.

The graph in **Figure 7a–f** shows the variation of  $M'$  with frequency at temperatures varying from 78 K to 253 K for different concentrations of Ag NPs added in CuTi-1223 superconductor. These plots show that  $M'$  exhibits lower values at lower frequencies and begin to increase gradually with the increase of frequency till it attains a maximum value  $M'_{Max}$  at certain specific frequency values for all concentrations of Ag NPs and temperatures. This demonstrate that ac-conduction in these composites is influenced by the short range mobility of carriers. The peaks in  $M'$  vs frequency plots at certain specific frequency values indicate the maximum conductance in the material, which can be attributed to the reduction in the capacitive reactance contribution to the total impedance of these composites. This is an evidence of the role of short-range mobility of carriers in transport phenomenon. The plots of  $M'$  vs  $f$  (Hz) shows that  $M'$  after attaining its maximum value at certain specific frequency starts to decrease indicating the transition from long range to short range mobility of carriers. The peaks observed in the  $M'$  versus frequency curves indicate a reduction in capacitive response, which is attributed to the maximum conductance reached within these composites. The gradual decrease in the values of  $M'_{Max}$ . With the increase of temperature indicates the enhancement of capacitive response, which is caused by the increase in the trapped space charges in the potential wells due to enhanced scattering of carriers across the grain-boundaries. The capacitive behavior has further been enhanced with the addition of Ag NPs in CuTi-1223 superconducting matrix. This is shown by insets of **Figure 7a–e**. The insets of **Figure 7a–e** and **Figure 7f** depict the variation of  $M'_{Max}$ . with temperature for various contents of Ag NPs in host CuTi-1223 superconducting matrix. The peaks shifted toward the higher frequency with increasing temperature is due to the fact that ac-conduction in these composites influenced by the short range mobility of charge carriers. The maximum conductance is produced in the material as a result of easy flow of charge carriers at greater temperature by increasing speed of these charge carriers which can be attributed to the reduction in the capacitive reactance contribution to the total impedance of these composites. This is also an evidence of the peak shifting to higher frequency with increasing temperature due to short-range mobility of carriers in transport phenomenon.

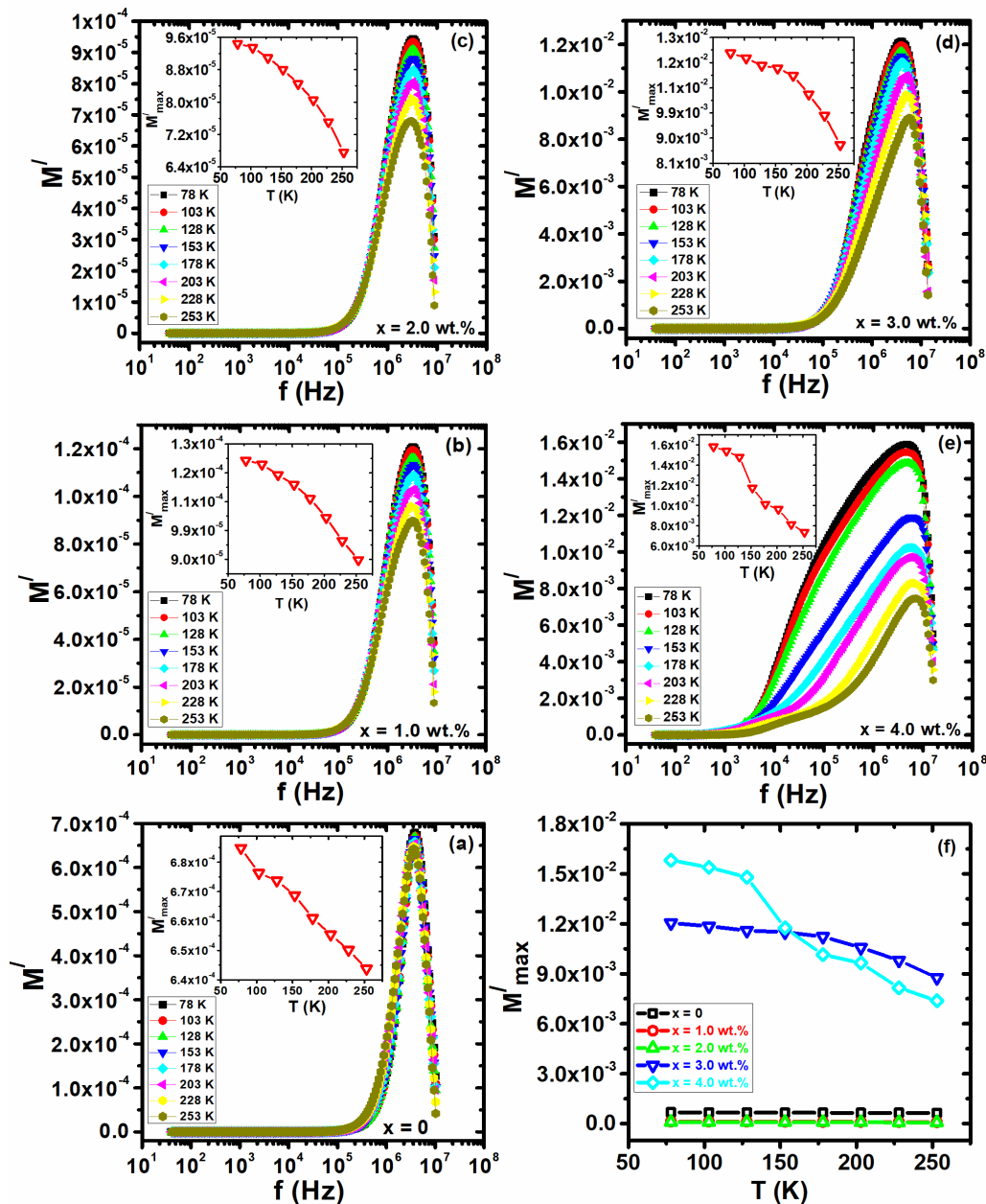


**Figure 7.** Variation in real part ( $M'$ ) of electric modulus versus test frequency  $f$  (Hz) from 40 Hz to 10 MHz at different operating temperatures  $T$  (K) from 78 K to 253 K for  $(\text{Ag})_x/\text{CuTi-1223}$  composites with (a)  $x = 0$ , (b)  $x = 1.0$  wt.%, (c)  $x = 2.0$  wt.%, (d)  $x = 3.0$  wt.%, (e)  $x = 4.0$  wt.% each with inset of variation in  $M'_{\text{Max}}$  versus  $T$  (K), and (f) combined variation of  $M'_{\text{Max}}$  versus  $T$  (K) for  $(\text{Ag})_x/\text{CuTi-1223}$ ;  $x = 0, 1.0, 2.0, 3.0$  and  $4.0$  wt.% composites.

The frequency-dependent changes in  $M'$  at different values of temperature from 78 K to 253 K for different concentrations of Ag NPs incorporated into CuTi-1223 superconductor are shown in **Figure 8a–f**. As the applied frequency increases, the  $M'$  values begin to rise and reach its maximum values at certain specific frequency values. After reaching its maximum value  $M'_{\text{Max}}$ , the  $M'$  values start to decrease, with the peaks shifting slightly towards lower frequency regions as the temperature rises. This pattern is an indication of the transition from long range mobility to short range mobility of charge carriers<sup>[37]</sup>. The insets in **Figure 8a–e** display the variations in  $M'$  values at specific frequencies as a function of temperature ( $T$  in Kelvin) for various concentrations of Ag NPs within the CuTi-1223 superconductor. **Figure 8f** illustrates the comparison of the changes in  $M'_{\text{Max}}$  with temperature ( $T$  in Kelvin) across different concentrations of Ag NPs within the CuTi-1223 superconducting matrix. The broadening in the peaks of  $M'$  versus frequency can be related to the non-

Debye nature of the relaxation processes occurring in these composites. The decreasing trend in  $M''_{\text{Max}}$  with increasing temperature values indicates the improvement in capacitive nature of the composites due to enhanced scattering and promoted trapping of charge carriers in the potential wells at the grain-boundaries. The change in  $M''_{\text{Max}}$  versus temperature shows the increasing trend in the  $M''_{\text{Max}}$  values particularly at higher contents of Ag NPs (i.e.,  $x = 3.0$  and  $4.0$  wt.%) in  $(\text{Ag})_x/\text{CuTl-1223}$  composites. This behavior revealed the improvement in conducting nature of the grain-boundaries because of the presence of metallic Ag NPs at the grain-boundaries causing the enhancement in conductance of the material<sup>[14]</sup>. The slight change in peak position in  $M''$  versus frequency curves can easily be understood from Equation (5) in terms of the variation in the values of  $C_{\text{gb}}$  and  $R_{\text{gb}}$  with temperatures as well as with Ag NPs addition in CuTl-1223 superconducting phase. The reduction in peak intensities with the increase of temperatures is referred to the growing capacitive response and suppression in ac-conduction phenomenon.

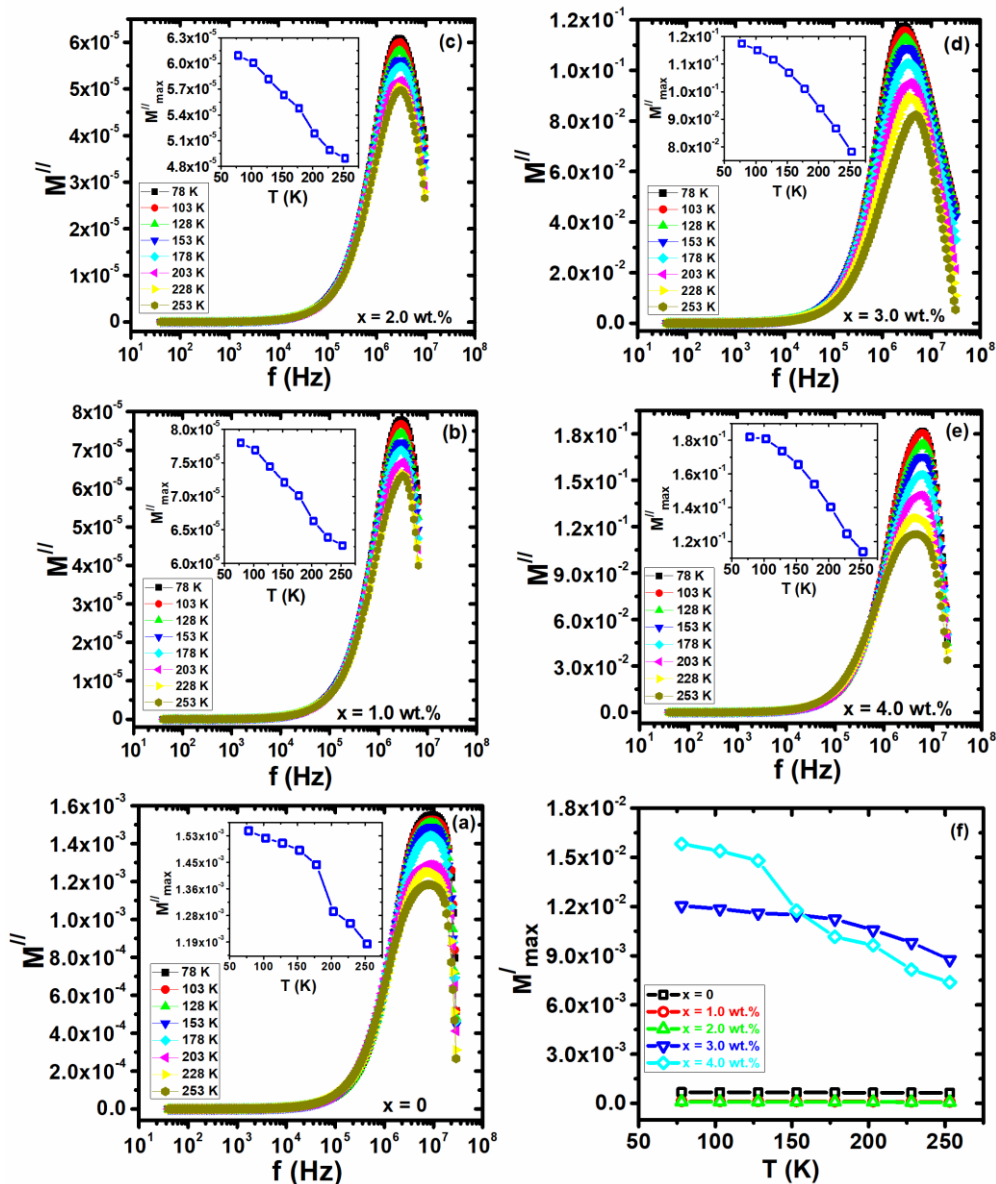


**Figure 8.** Variation in imaginary part ( $M''$ ) of modulus versus test frequency  $f$  (Hz) from 40 Hz to 10 MHz at different operating temperatures  $T$  (K) from 78 K to 253 K for  $(\text{Ag})_x/\text{CuTl-1223}$  composites with (a)  $x = 0$ , (b)  $x = 1.0$  wt.%, (c)  $x = 2.0$  wt.%, (d)  $x = 3.0$  wt.%, (e)  $x = 4.0$  wt.% each with inset of variation in  $M''_{\text{Max}}$  versus  $T$  (K), and (f) combined variation in  $M''_{\text{Max}}$  versus  $T$  (K) for  $(\text{Ag})_x/\text{CuTl-1223}$ ;  $x = 0, 1.0, 2.0, 3.0$  and  $4.0$  wt.% composites.

The Nyquist plots of  $M''$  versus  $M'$  for different concentrations of Ag NPs in these composites over a temperature range spanning from 78 K to 253 K are shown in **Figure 9a–e**. Nyquist plots are used to determine the values of  $C_g$ ,  $C_{gb}$  and total capacitance  $C (= C_g + C_{gb})$ . The  $C_g$  and  $C (= C_g + C_{gb})$  values can be obtained from left and right intercepts on  $M'$  axis of these Nyquist plots, respectively. The  $C_g$  and  $C_{gb}$  values for  $(Ag)_x/CuTi-1223$ ;  $x = 0 \sim 4.0$  wt.% composites at different temperatures are given in **Table 2**. The lower values of  $C_g$  in comparison to  $C_{gb}$  make it evident that the mobility of charge carriers experience fewer constraints within the grains than grain-boundaries, this can be attributed to the presence of impurities and different defects across the grain-boundaries<sup>[40]</sup>. The variations in the Nyquist plots as temperature rises reflects the multi-Debye relaxation phenomena occurring in these nanocomposites. The values of  $C_g$ ,  $C_{gb}$  and  $C$  have displayed a decreasing trend with the increasing temperature at various concentrations of Ag NPs. This trend can be attributed to the release of space charges, which were trapped at the inter-granular sites of the host material<sup>[39]</sup>.

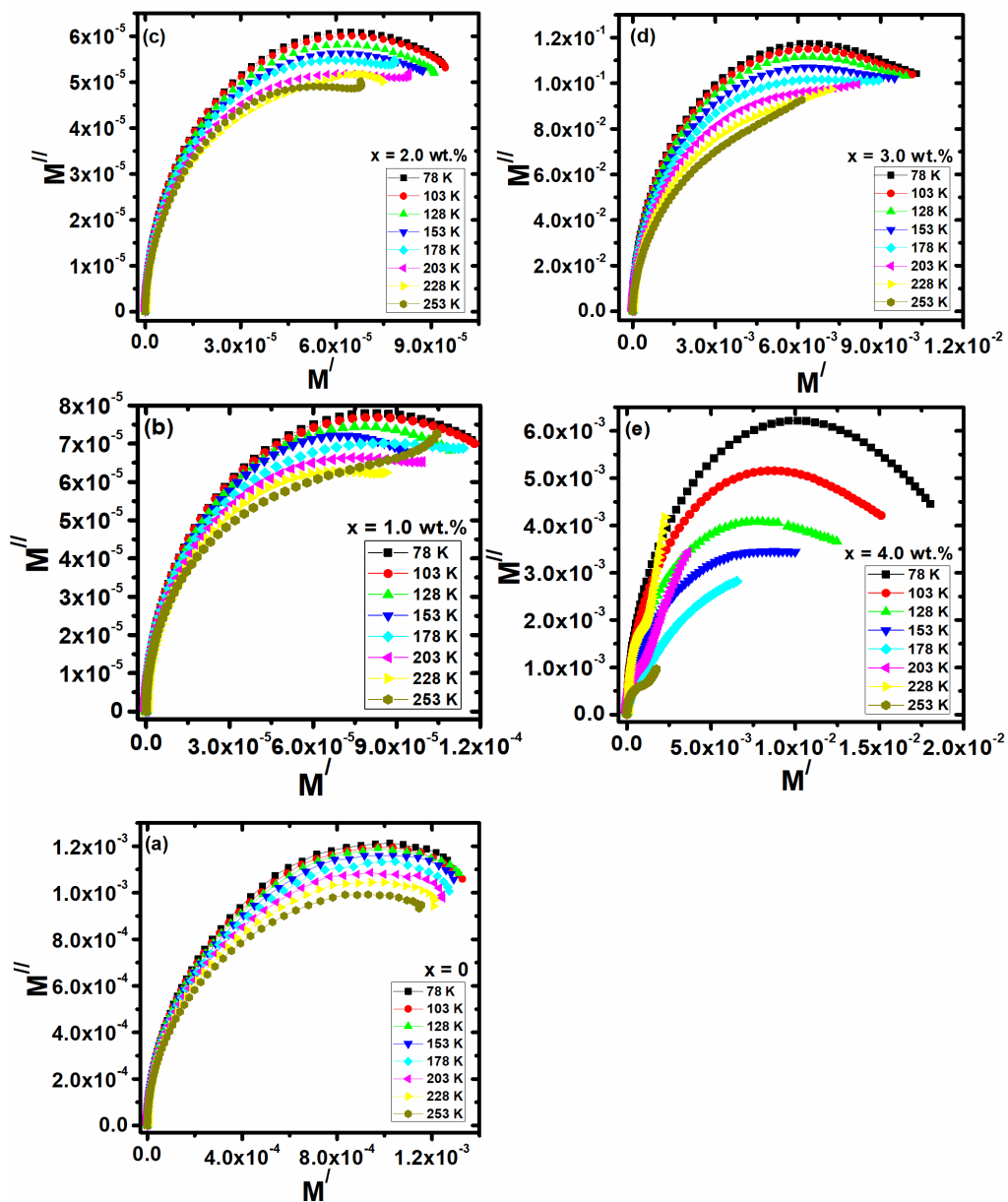


**Figure 9.** Nyquist plots between  $M'$  and  $M''$  at different operating temperatures  $T$  (K) from 78 K to 253 K for  $(Ag)_x/CuTi-1223$  composites with (a)  $x = 0$ , (b)  $x = 1.0$  wt.%, (c)  $x = 2.0$  wt.%, (d)  $x = 3.0$  wt.%, (e)  $x = 4.0$  wt.%.

**Table 2.** Calculated values of ' $C_g$ ' and ' $C_{gb}$ ' of  $(Ag)_x/CuTi-1223$ ,  $x = 0, 1.0, 2.0, 3.0$  and  $4.0$  wt.% composites at various temperatures.

<b><math>(Ag)_x/CuTi-1223</math>, <math>x = 0, 1.0, 2.0, 3.0</math> and <math>4.0</math> wt.% composites</b>										
<b>T (K)</b>	<b><math>x = 0</math></b>		<b><math>x = 1.0</math></b>		<b><math>x = 2.0</math></b>		<b><math>x = 3.0</math></b>		<b><math>x = 4.0</math></b>	
	<b><math>C_g</math> (nF)</b>	<b><math>C_{gb}</math> (mF)</b>								
78	0.068	1.27	0.038	0.116	0.015	0.934	0.029	10.3	0.044	18.0
103	0.049	1.33	0.040	0.117	0.015	0.944	0.038	10.1	0.084	15.1
128	0.075	1.31	0.042	0.109	0.018	0.909	0.042	9.91	0.013	12.4
153	0.089	1.29	0.041	0.930	0.017	0.873	0.042	9.50	0.013	12.4
178	0.082	1.27	0.054	0.113	0.017	0.783	0.044	8.93	0.017	6.52
203	0.043	1.24	0.042	0.990	0.015	0.829	0.030	8.15	0.069	3.61
228	0.020	1.21	0.053	0.862	0.018	0.747	0.028	7.23	0.054	2.25
253	0.051	1.15	0.043	0.104	0.022	0.676	0.023	6.14	0.063	1.74

## 4. Conclusion

This work reports the effects of Ag NPs on the ac- conduction mechanism of the CuTi-1223 superconducting phase by employing CIS and CEMS measurements. Improvement in the conduction properties was evident from the increasing trend in the values of  $R_g$  and  $R_{gb}$  with temperature. The decrease in capacitive characteristics seen in these nanocomposites as temperature rises is attributed to the discharge of space charge carriers trapped inside the potential wells. The occurrence of non-Debye type of relaxation processes in these composites was evident from the shifting of peaks in  $Z''$  and  $M''$  versus  $f$  (Hz) plots. The comparison of resistive and capacitive behavior of grains and grain-boundaries has confirmed that the contribution of grain-boundaries is dominant in these  $(Ag)_x/CuTi-1223$  composites.

## Author contributions

Conceptualization, MM, M, LA; methodology, MM, M, LA; formal analysis, MM, M, LA, AAK, HAA, MNK; data curation, AAK, HAA, MNK; writing—original draft preparation, MM, M, LA; writing—review and editing, MH; supervision, MM, M, LA. All authors have read and agreed to the published version of the manuscript.

## Conflicts of interest

The authors declare no conflict of interest.

## References

1. Sakhya AP, Dutta A, Sinha TP. Dielectric and impedance spectroscopic studies of neodymium gallate. *Physica B: Condensed Matter* 2016; 488: 1-7. doi: 10.1016/j.physb.2016.02.017
2. Thakur S, Rai R, Bdikin I, Valente MA. Impedance and Modulus Spectroscopy Characterization of Tb modified  $Bi_{0.8}A_{0.1}Pb_{0.1}Fe_{0.9}Ti_{0.1}O_3$  Ceramics. *Mat Res* 2016; 19(1): 1-8. doi: 10.1590/1980-5373-mr-2015-0504
3. Tian F, Ohki Y. Electric modulus powerful tool for analyzing dielectric behavior. *IEEE Trans Dielect Electr Insul* 2014; 21(3): 929-931. doi: 10.1109/tdei.2014.6832233
4. Macdonald JR. *Impedance Spectroscopy, Emphasizing Solid Materials and Systems*. John Wiley & Sons; 1987.
5. Bashir J, Shaheen R. Structural and complex AC impedance spectroscopic studies of  $A_2CoNbO_6$  ( $A = Sr, Ba$ ) ordered double perovskites. *Solid State Sciences* 2011; 13(5): 993-999. doi: 10.1016/j.solidstatesciences.2011.02.003
6. Kundu R, Roy D, Bhattacharya S. Microstructure, electrical conductivity and modulus spectra of  $CdI_2$  doped nanocomposite-electrolytes. *Physica B: Condensed Matter* 2017; 507: 107-113. doi: 10.1016/j.physb.2016.11.036

7. Padmamalini N, Ambujam K. Impedance and modulus spectroscopy of ZrO<sub>2</sub>-TiO<sub>2</sub>-V<sub>2</sub>O<sub>5</sub> nanocomposite. *Karbala International Journal of Modern Science* 2016; 2(4): 271-275. doi: 10.1016/j.kijoms.2016.10.001
8. Khan NA, Mumtaz M, Khurram AA. Frequency dependent dielectric properties of Cu<sub>0.5</sub>Tl<sub>0.5</sub>Ba<sub>2</sub>Ca<sub>2</sub>(Cu<sub>3-y</sub>Zn<sub>y</sub>)O<sub>10-δ</sub> (y = 0, 1.0, 1.5, 2.0, 2.5) superconductors. *J. Appl. Phys* 2008; 104: 033916.
9. Qasim I, Waqee-ur-Rehman M, Mumtaz M, et al. Role of anti-ferromagnetic Cr nanoparticles in CuTl-1223 superconducting matrix. *Journal of Alloys and Compounds* 2015; 649: 320-326. doi: 10.1016/j.jallcom.2015.05.288
10. Ali L, Mumtaz M, Ali I, et al. Metallic Cu Nanoparticles Added to Cu<sub>0.5</sub>Tl<sub>0.5</sub>Ba<sub>2</sub>Ca<sub>2</sub>Cu<sub>3</sub>O<sub>10-δ</sub> Superconductor. *J Supercond Nov Magn* 2017; 31(2): 561-567. doi: 10.1007/s10948-017-4229-8
11. Mohammed NH. Effect of MgO Nano-oxide Additions on the Superconductivity and Dielectric Properties of Cu<sub>0.25</sub>Tl<sub>0.75</sub>Ba<sub>2</sub>Ca<sub>3</sub>Cu<sub>4</sub>O<sub>12-δ</sub> Superconducting Phase. *J Supercond Nov Magn* 2011; 25(1): 45-53. doi: 10.1007/s10948-011-1207-4
12. Mumtaz M, Imran M, Khan MN. Frequency-Dependent Electric Modulus Spectroscopy of (Co<sub>3</sub>O<sub>4</sub>)<sub>x</sub>/(CuTl)-1223 Nanoparticles–Superconductor Composites. *Journal of Elec Materi* 2019; 48(6): 3588-3594. doi: 10.1007/s11664-019-07103-y
13. Mumtaz M, Naveed M, Amin B, et al. Temperature dependent impedance spectroscopy of (Co<sub>3</sub>O<sub>4</sub>)<sub>x</sub>/CuTl-1223 nanoparticles-superconductor composites. *Ceramics International* 2018; 44(4): 4351-4359. doi: 10.1016/j.ceramint.2017.12.029
14. Naveed M, Mumtaz M, Khan R, et al. Conduction mechanism and impedance spectroscopy of (MnFe<sub>2</sub>O<sub>4</sub>)<sub>x</sub>/CuTl-1223 nanoparticles-superconductor composites. *Journal of Alloys and Compounds* 2017; 712: 696-703. doi: 10.1016/j.jallcom.2017.04.034
15. Khan AA, Mumtaz M, Ali L, et al. AC Conduction Mechanism in (Cu)<sub>x</sub>/(CuTl)-1223 Nanoparticles–Superconductor Composites. *J Low Temp Phys* 2020; 199(5-6): 1268-1298. doi: 10.1007/s10909-020-02417-2
16. Qasim I, Waqee-ur-Rehman M, Mumtaz M, Nadeem K. Role of Co nanoparticles in CuTl-1223 superconductor. *Ceramics International* 2016; 42(1): 1122-1127. doi: 10.1016/j.ceramint.2015.09.040
17. Jabbar A, Qasim I, Khan KM, et al. Synthesis and superconducting properties of (Au)<sub>x</sub>/CuTl-1223 composites. *Journal of Alloys and Compounds* 2015; 618: 110-114. doi: 10.1016/j.jallcom.2014.08.162
18. Mumtaz M, Ali L, Khan MN, Sajid MU. Tuning of Dielectric Parameters of (NiFe<sub>2</sub>O<sub>4</sub>)<sub>x</sub>/CuTl-1223 Nano-superconductor Composites by Temperature and Frequency. *J Supercond Nov Magn* 2016; 29(5): 1181-1186. doi: 10.1007/s10948-016-3393-6
19. Waqee-ur-Rehman M, Qasim I, Mumtaz M, et al. Resistive transition and flux flow mechanism in CoFe<sub>2</sub>O<sub>4</sub> nanoparticles added Cu<sub>0.5</sub>Tl<sub>0.5</sub>Ba<sub>2</sub>Ca<sub>2</sub>Cu<sub>3</sub>O<sub>10-δ</sub> superconductor. *Journal of Alloys and Compounds* 2016; 657: 348-352. doi: 10.1016/j.jallcom.2015.10.112
20. Jabbar A, Qasim I, Waqee-ur-Rehman M, et al. Structural and Superconducting Properties of (Al<sub>2</sub>O<sub>3</sub>)<sub>y</sub>/CuTl-1223 Composites. *Journal of Elec Materi* 2014; 44(1): 110-116. doi: 10.1007/s11664-014-3405-x
21. Sahu T, Behera B. Investigation on structural, dielectric and ferroelectric properties of samarium-substituted BiFeO<sub>3</sub>-PbTiO<sub>3</sub> composites. *J Adv Dielect* 2017; 7(1): 1750001. doi: 10.1142/s2010135x17500011
22. Khan AA, Sohail M, Rahim M, et al. Frequency and temperature dependent dielectric constant of (Ag)<sub>x</sub>/CuTl-1223 nanoparticles-superconductor composites. *Journal of Alloys and Compounds* 2020; 825: 154138. doi: 10.1016/j.jallcom.2020.154138
23. Rabbani MW, Ali L, Mumtaz M, Hussain Gul I. Infield superconducting properties of nano-sized Ag added Cu<sub>0.5</sub>Tl<sub>0.5</sub>Ba<sub>2</sub>Ca<sub>2</sub>Cu<sub>3</sub>O<sub>10-δ</sub>. *Progress in Natural Science: Materials International* 2017; 27(4): 487-490. doi: 10.1016/j.pnsc.2017.06.011
24. Jabbar A, Qasim I, Mumtaz M, Nadeem K. Synthesis and superconductivity of (Ag)<sub>x</sub>/CuTl-1223 composites. *Progress in Natural Science: Materials International* 2015; 25(3): 204-208. doi: 10.1016/j.pnsc.2015.06.001
25. Jabbar A, Mumtaz M, Nadeem K. Noble metals (Ag, Au) nanoparticles addition effects on superconducting properties of CuTl-1223 phase. *Eur Phys J Appl Phys* 2015; 69(3): 30601. doi: 10.1051/epjap/2015140356
26. Hussain G, Jabbar A, Qasim I, et al. Activation energy and excess conductivity analysis of (Ag)<sub>x</sub>/CuTl-1223 nano-superconductor composites. *Journal of Applied Physics* 2014; 116(10). doi: 10.1063/1.4895051
27. Qasim I, Waqee-ur-Rehman M, Mumtaz M, et al. Ferromagnetic (Ni) nanoparticles–CuTl-1223 superconductor composites. *Journal of Magnetism and Magnetic Materials* 2016; 403: 60-67. doi: 10.1016/j.jmmm.2015.11.066
28. Sharma S, Shamim K, Ranjan A, et al. Impedance and modulus spectroscopy characterization of lead free barium titanate ferroelectric ceramics. *Ceramics International* 2015; 41(6): 7713-7722. doi: 10.1016/j.ceramint.2015.02.102
29. Kumari K, Ashutosh P, Kamal P. Dielectric, Impedance/Modulus and Conductivity Studies on [Bi<sub>0.5</sub>(Na<sub>1-x</sub>K<sub>x</sub>)<sub>0.5</sub>]<sub>0.94</sub>Ba<sub>0.06</sub>TiO<sub>3</sub>, (0.16 ≤ x ≤ 0.20) Lead-Free Ceramics. *American Journal of Materials Science* 2016; 6(1).
30. Sahoo PS, Panigrahi A, Patri SK, Choudhary RNP. Impedance and modulus spectroscopy studies of Ba<sub>3</sub>SrSmTi<sub>2</sub>V<sub>6</sub>O<sub>28</sub> ceramics. *Journal of Material Science* 2010; 28(763).

31. Nasri S, Ben Hafsia AL, Tabellout M, Megdiche M. Complex impedance, dielectric properties and electrical conduction mechanism of  $\text{La}_{0.5}\text{Ba}_{0.5}\text{FeO}_{3-\delta}$  perovskite oxides. *RSC Adv* 2016; 6(80): 76659-76665. doi: 10.1039/c6ra10589k
32. Lily, Kumari K, Prasad K, Choudhary RNP. Impedance spectroscopy of  $(\text{Na}_{0.5}\text{Bi}_{0.5})(\text{Zr}_{0.25}\text{Ti}_{0.75})\text{O}_3$  lead-free ceramic. *Journal of Alloys and Compounds* 2008; 453(1-2): 325-331. doi: 10.1016/j.jallcom.2006.11.081
33. Ahmad I, Akhtar MJ, Younas M, et al. Small polaronic hole hopping mechanism and Maxwell-Wagner relaxation in  $\text{NdFeO}_3$ . *Journal of Applied Physics* 2012; 112(7). doi: 10.1063/1.4754866
34. Belal Hossen M, Akther Hossain AKM. Complex impedance and electric modulus studies of magnetic ceramic  $\text{Ni}_{0.27}\text{Cu}_{0.10}\text{Zn}_{0.63}\text{Fe}_2\text{O}_4$ . *J Adv Ceram* 2015; 4(3): 217-225. doi: 10.1007/s40145-015-0152-2
35. Koops CG. On the Dispersion of Resistivity and Dielectric Constant of Some Semiconductors at Audiofrequencies. *Phys Rev* 1951; 83(1): 121-124. doi: 10.1103/physrev.83.121
36. Rahmouni H, Smari M, Cherif B, et al. Conduction mechanism, impedance spectroscopic investigation and dielectric behavior of  $\text{La}_{0.5}\text{Ca}_{0.5-x}\text{Ag}_x\text{MnO}_3$  manganites with compositions below the concentration limit of silver solubility in perovskites ( $0 \leq x \leq 0.2$ ). *Dalton Trans* 2015; 44(22): 10457-10466. doi: 10.1039/c5dt00444f
37. Liu J, Duan CG, Yin WG, et al. Large dielectric constant and Maxwell-Wagner relaxation in  $\text{Bi}_{2/3}\text{Cu}_3\text{Ti}_4\text{O}_{12}$ . *Phys. Rev. B* 2004; 70: 144106.
38. Venkataraman BH, Varma KBR. Microstructural, dielectric, impedance and electric modulus studies on vanadium—doped and pure strontium bismuth niobate ( $\text{SrBi}_2\text{Nb}_2\text{O}_9$ ) ceramics. *J Mater Sci: Mater Electron* 2005; 16(6): 335-344. doi: 10.1007/s10854-005-1144-8
39. Liu J, Duan CG, Yin WG, et al. Dielectric permittivity and electric modulus in  $\text{Bi}_2\text{Ti}_4\text{O}_{11}$ . *The Journal of Chemical Physics* 2003; 119(5): 2812-2819. doi: 10.1063/1.1587685
40. Roy A K, Prasad K, Prasad A. Piezoelectric, impedance, electric modulus and AC conductivity studies on  $(\text{Bi}_{0.5}\text{Na}_{0.5})_{0.95}\text{Ba}_{0.05}\text{TiO}_3$  ceramic. *PAC* 2013; 7(2): 81-91. doi: 10.2298/pac1302081r